Physics in Medicine & Biology

PAPER • OPEN ACCESS

Quantification of the tumour microvascular response to high dose-per-fraction radiotherapy

To cite this article: W Jeffrey Zabel *et al* 2025 *Phys. Med. Biol.* **70** 125015

IOP Publishing Phys. Med. Biol. 70 (2025) 125015 https://doi.org/10.1088/1361-6560/ade048

Physics in Medicine & Biology

IPEM Institute of Physics and Engineering in Medicine

OPEN ACCESS

RECEIVED
26 January 2025

REVISED
22 May 2025

ACCEPTED FOR PUBLICATION
3 June 2025

PUBLISHED
19 June 2025

PAPER

Quantification of the tumour microvascular response to high dose-per-fraction radiotherapy

W Jeffrey Zabel[1,*], Hector A Contreras-Sanchez[1], Nader Allam[1], Muhammad Mohsin Qureshi[2], Costel Flueraru[3], Edward Taylor[4,5] and I Alex Vitkin[1,4,5]

[1] Department of Medical Biophysics, University of Toronto, Toronto, ON, Canada
[2] Department of System Design Engineering, University of Waterloo, Waterloo, ON, Canada
[3] Advanced Electronic and Photonics Research Centre, National Research Council of Canada, Ottawa, ON, Canada
[4] Department of Radiation Oncology, University of Toronto, Toronto, ON, Canada
[5] Radiation Medicine Program, Princess Margaret Cancer Centre, Toronto, ON, Canada
[*] Author to whom any correspondence should be addressed.

E-mail: jeff.zabel@mail.utoronto.ca

Keywords: hypofractionated radiotherapy, tumour microenvironment, tumour microvasculature, functional optical coherence tomography, window chamber mouse model

Supplementary material for this article is available online

Abstract

Objective. Microvascular ablation during high dose-per-fraction radiotherapy (HDFRT) is disparately reported in the literature. This study was conducted to quantify the tumour microvascular response to different HDFRT schedules. *Approach*. A high single-dose irradiation of 20 Gy and two multifraction schedules (three fractions of 10 Gy and 15 Gy each) were studied. Patient-derived BxPC-3 pancreatic tumours in a mouse dorsal skinfold window chamber were treated and their 3D microvascular networks were longitudinally imaged with speckle variance optical coherence tomography for up to 7 weeks post irradiation. The overall vascular volume density (VVD), VVD for small vessels (diameters between 15–25 μm and 25–35 μm), and the vascular convexity index λ (a measure of vessel organization and space filling at short distances) were quantified. *Main results*. There were no significant differences in overall VVD for treated vs. control tumours at all timepoints. Examination of small-diameter vessels revealed some transient reductions in $VVD_{15-25\,\mu m}$ and $VVD_{25-35\,\mu m}$ compared to controls at $t \sim 3$ weeks for larger dose-per-fraction regimens (3×15 Gy and 1×20 Gy); ablated vasculature regrew back to baseline values by 7 weeks. Convexity indices for these larger-dose-per-fraction tumours were ~55% larger than unirradiated controls by the end of monitoring period; no such effects were seen in the 3×10 Gy cohort. *Significance*. The results of this study reveal the complex role of small vessels in microvascular ablation caused by HDFRT, with a dependence on the dose per fraction and total delivered dose. After small vessel ablation, regrown vessels had more uniform and regular spacing than non-ablated vessels as quantified by λ, potentially suggesting improved tumour response if subsequent retreatments are attempted.

1. Introduction

Advances in radiation therapy delivery and targeting technologies including image guidance, volumetric modulated arc therapy, and immobilization has enabled the safe delivery of much higher doses of radiation per fraction compared to the conventional low-dose high-fraction standard of care (Timmerman *et al* 2014). High-dose-per-fraction radiation therapy (HDFRT) including stereotactic radiosurgery and stereotactic body radiation therapy for extra-cranial lesions typically deliver 6–30 Gy per fraction in 1–5 fractions. The use of HDFRT has increased dramatically over the past decade owing to the decreased number of treatments which is more cost efficient and less time consuming for patients and staff (Timmerman *et al* 2014). Despite

radiobiological concerns over the potential for reduced tumour control, local control has largely remained high in tumours treated with HDFRT, perhaps owing to often elevated biologically effective doses (BEDs) as compared to standard conventionally fractionated regimens (Brown *et al* 2014, Park *et al* 2017).

Despite the increased use of HDFRT in the clinic, the exact mechanism of tumour cell kill in this treatment method is hotly debated (Brown *et al* 2014, Kozin 2022). Some researchers have argued that classical radiobiological modelling (linear quadratic model), including the effects of hypoxia, is sufficient to describe HFDRT tumour response (Carlson *et al* 2011, Brown *et al* 2014, Jeong *et al* 2017). However, others suggest that tumour microenvironmental changes, particularly microvascular ablation, are significantly affecting tumour cell kill, requiring new understanding beyond conventional DNA-damage mechanisms (Kirkpatrick *et al* 2008, Park *et al* 2012, Kim *et al* 2015).

Earlier studies found that single doses >8–10 Gy (Fuks and Kolesnick 2005) cause microvascular damage suggesting that tumour cell death may be partially caused by microvascular ablation, in addition to direct DNA damage (Fuks and Kolesnick 2005, Kirkpatrick *et al* 2008, Park *et al* 2012, Kim *et al* 2015). Despite these reports, several other studies found little to no functional microvascular loss in response to HDFRT (Moding *et al* 2013, Clément-Colmou *et al* 2020, Kaeppler *et al* 2022). This lack of scientific consensus may be attributed to differences in experimental protocols (animal model, radiation delivery, cell line, immune status, etc) and microvascular quantification methods. Kozin *et al* attempted to build a model of microvascular ablation and regrowth after irradiation based on the often-conflicting published findings (Kozin *et al* 2012). This work demonstrated the urgent need for more advanced imaging technologies for tracking microvascular changes in response to HDFRT.

Despite various available imaging modalities, most do not possess the necessary spatial resolution, contrast, nor suitability for long term repetitive microvascular imaging. For example, power Doppler ultrasound can image the microvasculature in 3D but with imaging resolution of $\sim 100\ \mu$m (Moran and Thomson 2020). Micro CT exhibits good imaging resolution in the range of $3-50\ \mu$m but requires significant doses of ionizing radiation and contrast agent administration, making it unsuitable for repetitive imaging (Clark and Badea 2021). Perfusion MRI/CT rely on indirect measurements of the vasculature, deriving vascular metrics via compartmental modelling (Cuenod and Balvay 2013). Optical microscopy techniques such as confocal and multiphoton microscopy have excellent resolution ($< 5\ \mu$m) but are limited to a depth of penetration $<\ 400\ \mu$m and typically long imaging times owing to their point-scanning nature (Lin *et al* 2023). They also require the use of fluorescently labelled contrast agents that can be toxic, accumulate in the tissue, and induce perturbations in the tissue microenvironment making them unsuitable for long term imaging (Jensen 2012). Photoacoustic microscopy requires no contrast and can image in 3D with excellent resolution ($\sim 3\ \mu$m) and reasonable depth penetration ($\sim$1 mm) (Liu and Wang 2022). However, achieving the same resolution across varying depths is challenging and direct physical contact with the imaged tissue is required.

Optical coherence tomography (OCT) is a high-resolution 3D optical imaging modality capable of imaging subsurface tissue morphology and function. Speckle variance OCT (svOCT) is its functional extension that detects tissue microcirculation by the decorrelation in signal of moving scatterers (red blood cells) compared to static tissue, using repetitive structural image acquisitions (Mariampillai *et al* 2008). svOCT, previously validated with confocal fluorescence microscopy (Mariampillai *et al* 2008, 2010), can image microvasculature to a depth of $\sim$2 mm into tissue in 3D over large fields of view (several square mm or even cm). Importantly, in the context of repeated longitudinal imaging, no contrast agents are required so no toxic accumulations occur. svOCT has been used in several preclinical studies (Demidov *et al* 2018a, 2018b, Allam *et al* 2022) to longitudinally quantify radiation-induced microvascular changes.

svOCT has been recently used by our group (Demidov *et al* 2018a) to validate Kozin *et al*'s theoretical model of microvascular changes after high single fraction irradiations (Kozin *et al* 2012). We noted a dose dependent loss in overall vascular volume density (VVD) followed by regrowth in the VVD to its pre-irradiation levels (Demidov *et al* 2018a). In the current study, we continued this research by testing the tumour response to more clinically relevant *multifraction* HDFRT treatment regimes. We employed svOCT to quantify tumour microvasculature longitudinally in a dorsal skinfold window chamber (DSWC) tumour mouse model (Zabel *et al* 2024). The DSWC tumour mouse model enables direct visualization of the tumour microenvironment through a surgically implanted glass window and permits longitudinal imaging for up to 10 weeks (Zabel *et al* 2024). DSWC models have been used for over 80 years in preclinical microvascular research providing valuable insight into treatment induced microvascular changes (Menger *et al* 2002, Schreiter *et al* 2017).

In this study, we thus quantified the longitudinal microvascular response to a single high dose irradiation of 20 Gy, and two multi-fraction irradiation schedules: three fractions of 10 Gy, and three fractions of 15 Gy. In our previous work, the 1×20 Gy regimen has been shown to produce clear vascular ablation in

pre-clinical tumour models (Demidov *et al* 2018a). The 3 × 10 Gy regimen has the same equivalent BED as 1 × 20 Gy for early-responding tissues (assuming $\alpha/\beta = 10$ Gy^{-1}), 60 Gy_{10}, albeit using a more clinically-relevant fractionation. Typical HDFRT regimens for pancreatic, liver, prostate, and lung cancers employ BEDs of 60–120 Gy_{10}; the 3 × 15 Gy regimen explored in our study (BED = 113 Gy_{10}) is thus representative of the higher end of this range.

From the obtained microvascular images, two important biometrics were extracted. The VVD (the proportion of tissue occupied by vessels), a biometric widely used in histology (Park *et al* 2012) and svOCT (Demidov *et al* 2018a, 2018b), provided an overall measurement of tumour vascularity. Importantly, its further refinement for different size vessels quantified HDFRT effects as a function of vessel diameter. The vascular distribution convexity index (Baish *et al* 2011, Allam *et al* 2022) was calculated to report on the functional efficiency of the microvascular networks. It reflects microvascular organization, with higher values indicating well-ordered vessels (typical for healthy tissues) and lower values indicating disorganized microvascular structure with inefficient delivery of nutrients and oxygen to surrounding tissues (typical for tumours) (Baish *et al* 2011).

2. Methods

2.1. Tumour cell inoculation and animal model

Anesthesia for all procedures was done with 5% isoflurane for induction, 2% for maintenance with 0.5 l min^{-1} oxygen flow rate. Human pancreatic cancer cells (BxPC-3) transfected with DsRed (Tan *et al* 1986) were grown in RPMI 1640 medium (Gibco, ON, Canada) with 10% foetal bovine serum and 1% Penicillin/streptomycin, starting two weeks prior to inoculation. Cells were incubated at 37 °C and 5% CO_2. For inoculation, ∼250 000 cells were suspended in a 1:1 mixture of phosphate buffered saline and Matrigel (BD Biosciences, ON, Canada) with a total volume of 20 μl. The suspension was then injected subcutaneously into the dorsal skin of 7–8 week-old immunodeficient NOD-Rag1^{null} IL2rg^{null} (NRG) female mice with a 29-gauge syringe. More preparation details can be found in (Zabel *et al* 2024).

To allow the tumour to develop a realistic 3D shape, the tumour was grown in the bare skin until it reached a diameter of ∼3–5 mm (3–4 weeks post inoculation) (Maeda and DaCosta 2014). Mice were then anesthetised and custom 3D-printed biocompatible plastic window chambers with a glass coverslip were surgically sutured to the dorsal skin as described previously (Zabel *et al* 2024) (figure 1(A)). The DSWC includes spacers between the two frames to maintain a constant low pressure on the skin flap to allow adequate tumour blood flow. Tumour imaging commenced 5 d post-surgery to allow for animal recovery.

2.2. OCT imaging and optical microscopy

For imaging, mice were anesthetised and secured to a custom 3D-printed animal holder with built-in electric heater to maintain body temperature at 37 °C (Zabel *et al* 2024). Brightfield (figure 1(B)) and DsRed fluorescence (figure 1(C)) imaging were performed for tumour localization and viability assessment, using an epifluorescence microscope (Leica Microsystems MZ FLIII, Richmond Hill, ON, CA) with consistent exposure times.

For microvascular quantification, svOCT images were acquired using a previously described swept-source OCT imaging system (Mao *et al* 2008, Demidov *et al* 2018a). 24 B-scans (axial scans) were acquired per location (25 ms apart) over a 6 × 6 mm^2 field of view (1600 total spatial locations). The axial and lateral resolutions in air were 8 μm and 15 μm respectively. Figure 1(D) shows the structural image obtained from averaging the 24 B-scans per location. To generate the svOCT dataset, the interframe intensity variance was calculated (Mariampillai *et al* 2008) to obtain figure 1(E). Figures 1(F) and (G) shows further refinement for different (small) vessel diameters.

2.3. Tumour and microvascular segmentation

All imaging data was processed using MATLAB (Mathworks, Natick, MA). First, the brightfield and fluorescence images were coregistered to the OCT dataset using point based affine registration based on vascular landmarks (Jenkinson and Smith 2001). To define the lateral extent of the tumour in the OCT volume, Otsu's thresholding (Otsu 1979) was performed on the coregistered fluorescence image (solid white line in figure 1(C)) then transposed to all the other optical images. To calculate the tumour volume, the tumour was manually contoured in the axial (depth) direction on the structural OCT B-scans (figure 1(D)). If the tumour extended past the maximum imaging depth, an OCT structural image from the backside of the window chamber was acquired for tumour volume estimation.

To restrict microvascular quantification to the highest SNR svOCT signal regions, an 'analysis region' was defined to encompass the first 500 μm below the glass coverslip of the tumour contour (dotted blue line in figures 1(D)–(G)). For 3D microvascular segmentation, the following steps were sequentially performed:

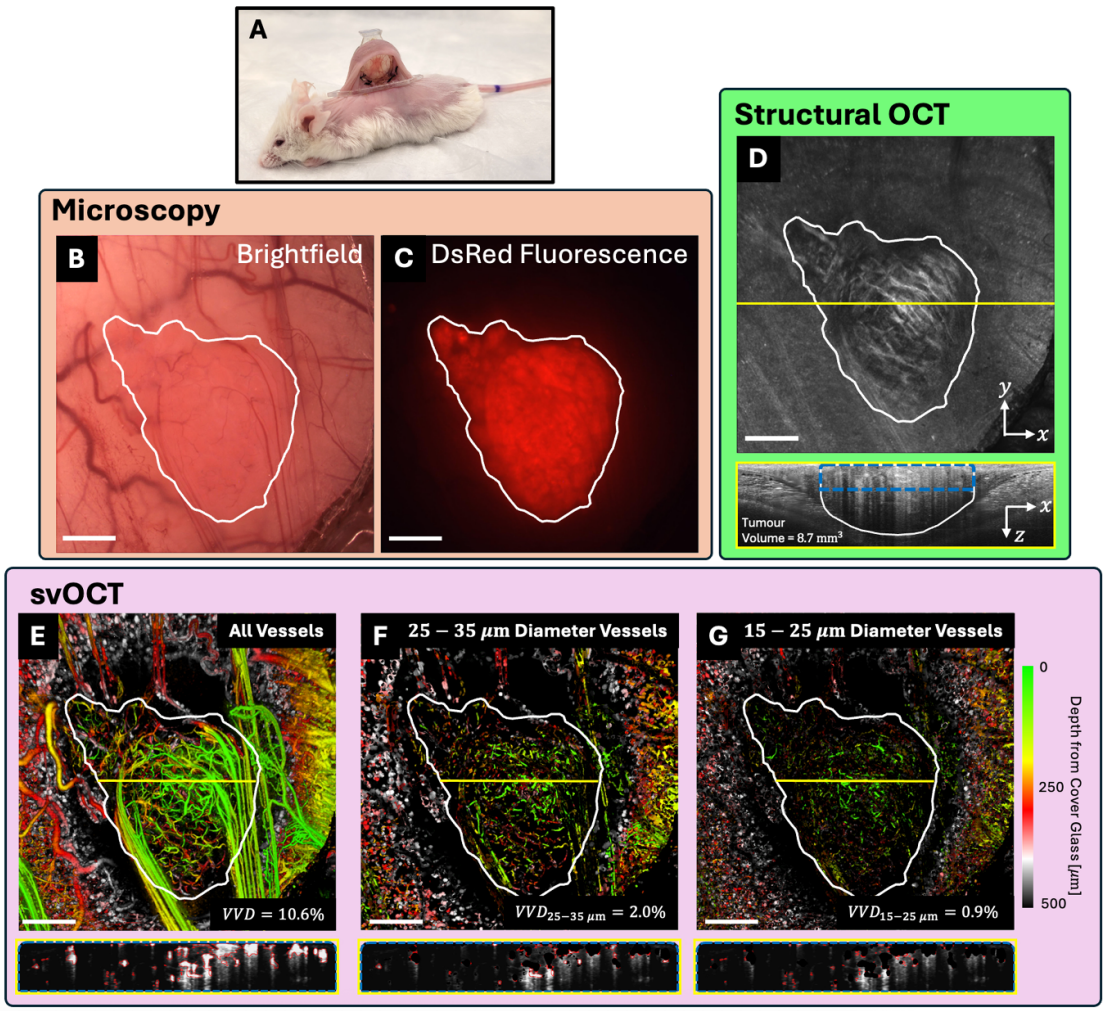

Figure 1. Optical *in-vivo* imaging and quantification. (A) A mouse dorsal skinfold window chamber xenograft tumour model, 5 d post-surgery. This animal model facilitates longitudinal brightfield (B), fluorescence (C), structural OCT (D), and svOCT microvascular imaging (E) with further refinements for different vessel diameters (F)–(G). Panels (B)–(G) are co-registered with each other. The white tumour contour derived from the fluorescence image (C) is shown in (B)–(G). In (D)–(G), an example B-scan taken from the yellow line region is shown in the bottom portion of each panel. An analysis region (indicated by the dotted blue line in D, lower panel) is defined as the first 500 μm in depth of the tumour contour below the glass coverslip. Microvascular segmentations are shown with the red contours in the example B-scans in (E)–(G). Scale bar = 1 mm. (A) Reproduced with permission from Zabel *et al* (2024).

denoising, contrast enhancement, deshadowing, and binarization. The denoising, contrast enhancement, and binarization steps were performed on each lateral *en-face* C-scan (to maintain consistent signal depth attenuation). For denoising, a low pass Gaussian filter to reduce background noise, and a median filter to reduce 'salt and pepper' speckle noise, were applied (Vakoc *et al* 2009, Conroy *et al* 2012, Casper *et al* 2019). A top hat filter was then used to enhance contrast (Mendonça and Campilho 2006). The forward scattering by red blood cells at 1300 nm causes long 'shadowing' artefacts. To minimize these, a step-down exponential filter for each axial A-scan was used as described in (Vakoc *et al* 2009); this filter attenuates the underlying voxels by a numerical factor proportional to the sum of the voxels immediately above. For binarization, Otsu's thresholding (Otsu 1979) was applied (Conroy *et al* 2012, Casper *et al* 2019). The overall resultant vessel segmentation accuracy was manually verified and corrected if necessary. The vascular segmentation quality is demonstrated in the colour depth-encoded svOCT microvascular image and representative B-scan (with overlaid vessel segmentations in red) in figure 1(E).

2.4. Microvascular metric calculation

The overall VVD was calculated as the proportion of the analysis region occupied by vessels (figure 1(E)). To calculate the microvascular density of specific vessel diameters, a 3D morphological opening operation was performed using a spherical structuring element to isolate vessels of a specified diameter (Fitzpatrick and Sonka 2000). Figures 1(F) and (G) shows the results of this vessel diameter selection operation for vessels with a diameter between 25 – 35 μm and 15 – 25 μm respectively.

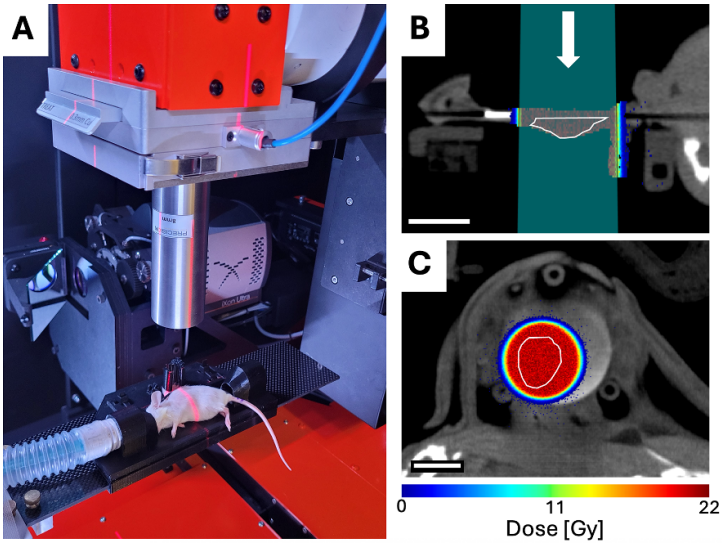

Figure 2. Tumour irradiation. (A) The mouse was secured to a motorized stage and 3D printed immobilization device under the microirradiator. (B), (C) An example of the dose distribution for a 20 Gy treatment, shown in the axial and sagittal planes respectively; the tumour is contoured with the white line. (B) Shows the radiation beam (light blue) with the direction indicated by the white arrow. (B), (C) Scale bar = 5 mm.

For convexity analysis, the distance to the nearest vessel, δ, was calculated for each non-vascular voxel in the analysis region by applying a Euclidean distance transform on the segmented dataset. A log–log plot of the normalized distance to nearest vessel histogram, $n(\delta)$, with 10 μm bin sizes was generated. The convexity index λ was defined as the slope of the linear portion of the curve up to a distance of 40 μm (Baish *et al* 2011, Allam *et al* 2022).

2.5. Irradiation

A small animal irradiator (X-Rad SmART+, Precision X-Ray, Madison, CT) was used for HDFRT (figure 2(A)). Mice were anesthetised and secured to a custom 3D-printed stage. A cone beam computed tomography image was obtained. The tumour was manually contoured and Monte Carlo treatment planning was performed (SmART-ATP V2.2.20230421, SmART Scientific Solutions B.V., Maastricht, Netherlands) (van Hoof *et al* 2013) for a single beam positioned perpendicular to the DSWC (figures 2(B) and (C)). The plan was delivered using 225 kV x-rays with an 8 mm circular collimator and copper filter. Dose was verified by Gafchromic film (EBT3, Ashland Advanced Materials, Bridgewater NJ) placed on the DSWC.

2.6. Imaging and irradiation schedule

Tumours were imaged every 3–4 d for two weeks after DSWC surgery to monitor the pre-irradiation tumour growth and microvascular development. Animals were then randomly assigned to one of four groups: unirradiated controls ($n = 10$), 1 fraction of 20 Gy ($n = 9$), 3 fractions of 10 Gy/fraction ($n = 10$), or 3 fractions of 15 Gy/fraction ($n = 11$). During the week of irradiation, animals were imaged on day 0 (first fraction on Monday), day 2 (second fraction on Wednesday), and day 4 (third and final fraction on Friday). All imaging on days of irradiation was done before the treatment. Mice were then imaged every 3–4 d up to 7 weeks or until humane endpoint was reached. Over the time course of the study the animal numbers per group dropped somewhat, most commonly due to window chamber wear. The number of animals per treatment group at each time point is shown in the supplementary data file. A minimum of four mice per treatment group was used before terminating the experiment.

2.7. Statistical analysis

Longitudinal plots are displayed as the percentage change relative to the day 0 pre-irradiation time point. Mathematically, for a metric value y at timepoint t: $y_{\text{display}}(t) = \frac{y(t)-y(0)}{|y(0)|} \times 100\%$. A linear mixed-effects model with random intercepts was used to assess whether each treatment group differed significantly from the unirradiated control group at each time point, with time treated as a categorical variable (Gueorguieva and Krystal 2004). Bonferroni correction was applied to adjust for multiple comparisons. A p-value < 0.05 was considered significant. All data points were represented as mean $\pm$ standard error of the mean (SEM).

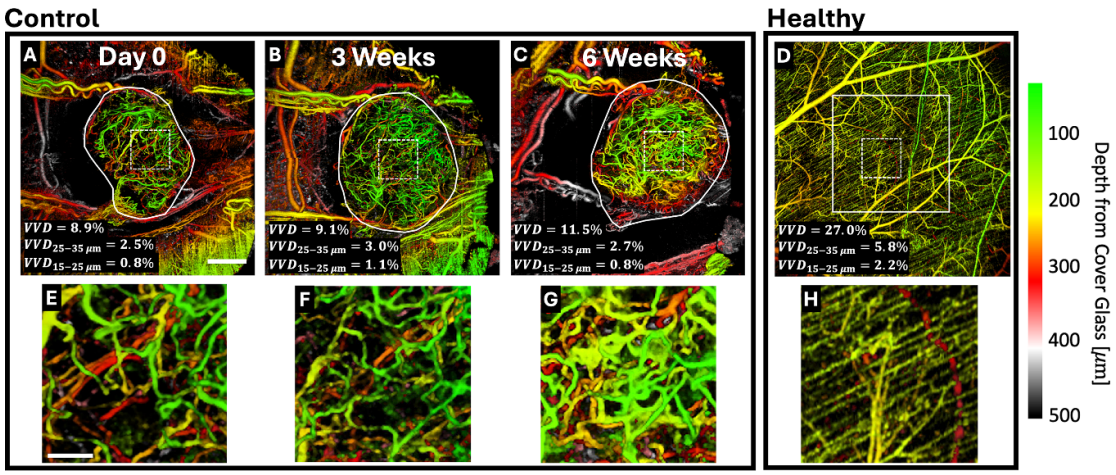

Figure 3. Colour depth encoded svOCT maximum intensity projections for an unirradiated control tumour and healthy bare-skin mouse. A representative unirradiated control tumour is shown at day 0 (A), 3 weeks (B), and 6 weeks (C). A healthy bare-skin mouse is shown (D) for comparison. The solid white line in (A)–(C) indicates the tumour boundary and in (D) it represents the typical lateral extent of a tumour. VVD values are calculated within the tumour boundary or comparable volume in the case of the healthy tissue and displayed in (A)–(D). (E)–(H) show a zoomed in region indicated by the white dotted line in (A)–(D). (A)–(D) Scale bar = 1 mm, (E)–(H) = 250 μm.

3. Results and discussion

3.1. Tumour volume, fluorescence, and microvascular density response to HDFRT

Figure 3 shows svOCT microvascular images of a representative non-irradiated control tumour (figures 3(A)–(C) and (E)–(G)) and a 'healthy' non tumour bearing bare skin mouse (figures 3(D) and (H)) for comparison. Images of the control tumour are shown at Day 0, 3 weeks, and 6 weeks, to illustrate the typical microvascular progression over the monitoring period. The top row in figure 3 shows the entire 6×6 mm^2 imaging field of view with a solid white line indicating the tumour boundary. In the case of the healthy bare-skin mouse, the solid white line represents the typical lateral extent of a tumour ($\sim 3 \times 3$ mm^2) (figure 3(D)). The overall VVD, $VVD_{25-35\,\mu m}$, and $VVD_{15-25\,\mu m}$ were calculated over the entire tumour region (for the healthy mouse, within the solid white line volume of interest) and are displayed at the bottom of each panel. Over the course of the monitoring period, the tumour grew as indicated by the increasing diameter of the tumour boundary (figures 3(A)–(C)). In terms of the microvascular progression of this tumour, there was a 29% increase in VVD from day 0–6 weeks and vessels with diameters between 25 and 35 μm experienced an 8% increase. Vessels with diameter between 15–25 μm remained unchanged in vascular density. The overall increase in vascular density over time is typical of growing tumours since they excrete excessive levels of VEGF to recruit new vessels to support their continued growth (Ferrara 2005). This causes the formation of a highly abnormal vascular network compared to healthy tissue (figures 3(D) and (H)). The healthy mouse had a higher calculated VVD across all vessel diameter bins compared to the control tumour. This vascular deterioration is typical in pancreatic tumours which often exhibit poorly perfused hypoxic regions (Conroy *et al* 2012, Metran-Nascente *et al* 2016). Note that although the healthy skin may appear visually less vascularized than the tumour, it is only ~ 350 μm thick and so less tissue was being imaged in depth compared to the considerably thicker tumours.

A representative tumour from each of the three HDFRT treatment schedules is shown in figure 4. All tumours are shrinking in size because of the treatment as shown by the decrease in diameter of the solid white tumour boundary from day 0–6 weeks. However, the microvascular response of these tumours is markedly different depending on the fractionation schedule. For instance, the 1×20 Gy treated tumour (figures 4(A)–(C)) had a slight decrease in the overall VVD over time compared to the control tumour that exhibited steadily increasing values of the VVD metric. This suggests that the microvascular growth is stalled by the treatment, causing a 'vascular growth arrest'. Focusing on smaller vessels, we found a 13% reduction in $VVD_{25-35\,\mu m}$ and $VVD_{15-25\,\mu m}$ by 3 weeks (figure 4(B)) and these small vessels regrew back to their baseline values by 6 weeks (figure 4(C)). Figure 4(B) shows that large vessels (blue arrows) are not impacted by the treatment whereas small vessels (red arrows) are ablated at 3 weeks.

Although the 1×20 Gy and 3×10 Gy regimens have approximately the same BED (for early effects), the microvascular responses to these two treatments were dramatically different. Surprisingly, the 3×10 Gy

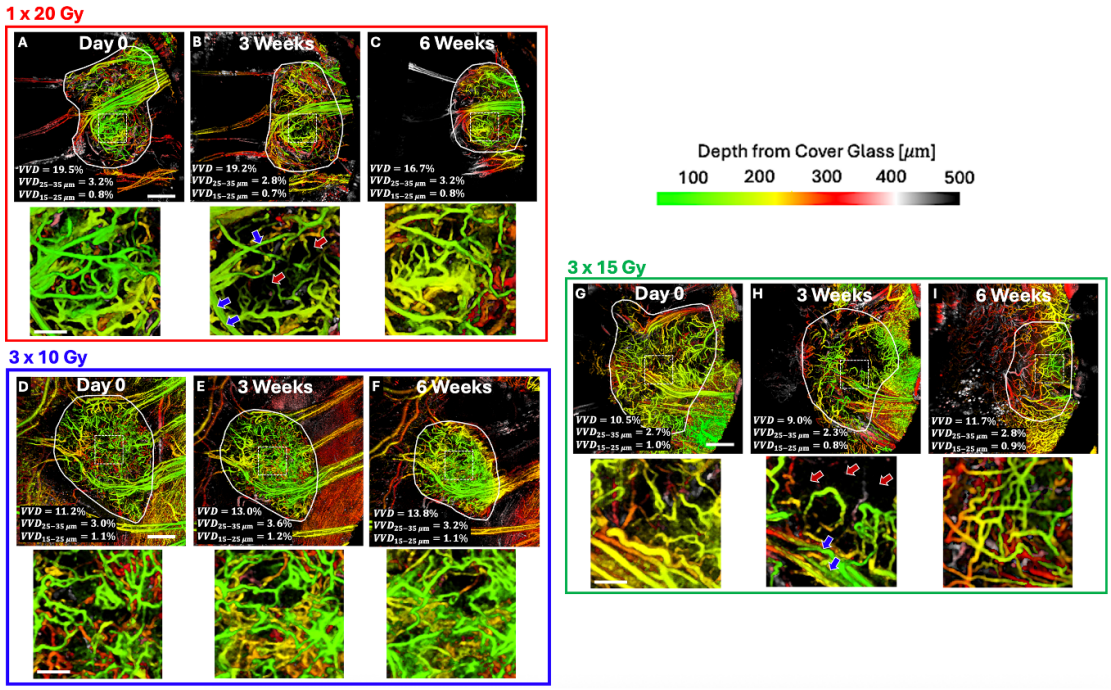

Figure 4. Colour depth encoded svOCT maximum intensity projections for the examined HDFRT fractionation schedules. A representative tumour is shown for 1 × 20 Gy (A)–(C), 3 × 10 Gy (D)–(F), and 3 × 15 Gy (G)–(I) treatments. Each time point shows the entire tumour volume as well as a zoomed in region directly below (for the region indicated by the white dotted line). The solid white line represents the tumour boundary. VVDs are calculated within the tumour boundary and displayed for each timepoint. In the zoomed-in panels, blue arrows indicate unaffected large vessels and red arrows indicate ablated small vessels. (A)–(I) Scale bar = 1 mm, zoomed-in panels = 250 μm.

treated tumour showed no loss in the microvasculature but an actual increase in VVD for all vessel diameter bins over time (figures 4(D)–(F)), indicating ineffective vascular ablation for this treatment regimen.

In contrast, the 3 × 15 Gy treated tumour (figures 4(G)–(I)) exhibited a 14% drop in overall VVD, with a 15% drop in $VVD_{25-35\,\mu m}$ and 20% drop in $VVD_{15-25\,\mu m}$ by 3 weeks. This is clearly shown in figure 4(H) where small vessels (red arrows) are ablated whereas large vessels (blue arrows) are unaffected. Similar to the 1 × 20 Gy treated tumour, these small vessels regrew back to their pre-irradiation VVD levels by 6 weeks (figure 4(I)).

These selected tumours are useful for representative visualization of the complex microvascular changes that are occurring during tumour development and progression (figure 3) and the three treatment schedules (figure 4). The added benefit of our svOCT imaging and analysis platform is its ability to image and quantify the microvascular response of large cohorts of mice longitudinally over several weeks of monitoring time. We thus present the results for our entire 40-mice dataset in figure 5.

Looking at the non-vascular compartment response first, the change in tumour volume is shown in figures 5(A) and (B) shows the DsRed fluorescence intensity which is a measure of tumour cell viability (Suetsugu *et al* 2012). Control mice (black line) showed a gradual increase in the tumour volume and viability over time, indicating expected disease progression in the absence of treatment. There was a short growth delay that occurred around the 0–4 week interval, possibly caused by an immature microvascular network that failed to support the rapid growth of the tumour as previously reported (Muz *et al* 2015). As the microvascular network continues to mature to meet the needs of the tumour cells, its growth can then continue. This argument is supported by the drop and stagnation of $VVD_{15-25\mu m}$ in the 0–2 week timepoints for control mice (figure 5(E)). Then at 2–4 weeks, there is a rise in $VVD_{15-25\mu m}$ (figure 5(E)) indicating more vascular supply to the tumour cells, allowing the tumour to enter a rapid growth phase starting at ∼4 weeks (figure 5(A)).

All irradiated mice experienced a decrease in tumour volume (figure 5(A)) and fluorescence (figure 5(B)) following irradiation. At 7 weeks there was no statistical differences between any of the treated groups (tumour volume: $p = 0.34$, fluorescence: $p = 0.65$) indicating that the three treatment regimen are approximately equivalent in eliciting a similar response over the 7 week observation window. It is not surprising that the radiobiologically-equivalent 1 × 20 Gy and 3 × 10 Gy schedules yield similar tumour volume responses; however we might expect to see a difference for the 3 × 15 Gy treated mice. A potential explanation for this is that the full-time course of tumour changes was not observed over the 7 week

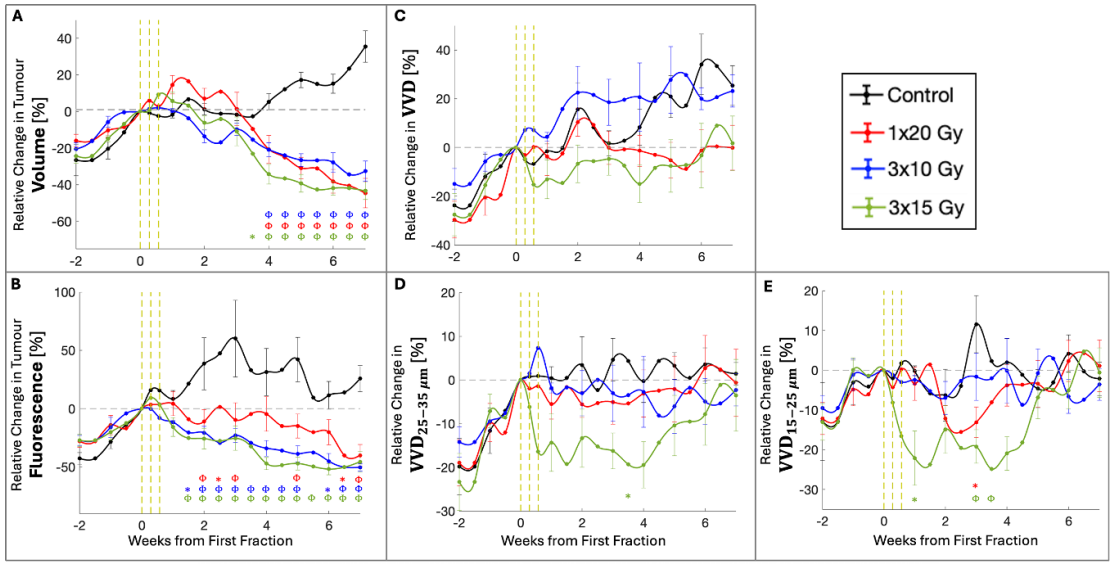

Figure 5. Quantification of tumour volume, fluorescence, and microvascular response to HDFRT. The relative percentage change in tumour volume (A), tumour fluorescence (B), vascular volume density (C), vascular volume density of vessels with diameter between 25 μm and 35 μm (D), and vascular volume density of vessels with diameter between 15 and 25 μm (E). All metrics are displayed as a percentage change relative to their day 0 pre-irradiation measurement. The yellow dotted lines indicate the timepoints at which radiation was delivered. Points are mean values with error bars ±SEM. The symbols represent significant differences of the treatment cohorts vs. controls with the following significance levels: $^{*}p < 0.05$, Φ $p < 0.01$.

monitoring time. These findings can be compared to our previous work (Demidov *et al* 2018a) where tumours grew at an average rate of 2.9%/day, whereas the tumours in the current study grew slower at an average rate of 1.3%/day. This change in tumour growth rates may be caused by the differences in the window chambers. Here we used a custom designed 3D printed window chamber (Zabel *et al* 2024) compared to a titanium window chamber model previously employed (Demidov *et al* 2018a). We are intentionally using plastic DSWCs since these are MR-compatible; in view of potential clinical translation, we are investigating the linkages between svOCT and perfusion MRI metrics to assess whether perfusion MRI can measure HDFRT-induced microvascular changes directly detectable by svOCT (Zabel *et al* 2022, 2024). Overall, the plastic DSWC design seems to slow down tumour growth, actually better approximating 'normal' disease progression (these tumours take several months to grow in humans). This slower growth rate likely manifests as slower response to treatment, which thus may or may not be fully captured in our 7 week-post-treatment observation period. Another potential explanation for the similarity in tumour volume responses is radiobiological saturation, whereby the lower BED treatments (3 × 10 Gy and 1 × 20 Gy) were already maximally effective, so further increases in BED would not yield additional tumour volume reduction.

Figure 5(C) shows the overall VVD response for control and treated tumours. There were no statistically significant differences identified at any time point; however, the subtle trends of the data may offer some useful insight. Specifically, control tumours had a gradual increase in VVD over time which is expected since growing tumours promote angiogenesis to support the tumour growth via excessive VEGF excretion (Muz *et al* 2015, Metran-Nascente *et al* 2016). The 3 × 10 Gy treated tumours also exhibited a gradual increase in VVD over the monitoring period with a similar trend to control mice. The higher dose per fraction treatments (1 × 20 Gy and 3 × 15 Gy) did exhibit a different trend than control and 3 × 10 Gy treated tumours. In 1 × 20 Gy cohort, the treatment seemed to arrest VVD increase. The 3 × 15 Gy treated tumours showed a decrease in VVD by ∼15% from baseline in the 1–5 week timeframe; this was followed by regrowth back to baseline values by 7 weeks.

Small vessels are likely more impacted by high dose radiation (Demidov *et al* 2018a, Kaeppler *et al* 2022) so $VVD_{25-35\,\mu m}$ (figure 5(D)) and $VVD_{15-25\,\mu m}$ (figure 5(E)) may be more meaningful metrics. The 3 × 10 Gy treated tumours again showed no significant differences compared to controls in $VVD_{25-35\,\mu m}$ (figure 5(D)) and $VVD_{15-25\,\mu m}$ (figure 5(E)). Mice that were treated with the higher doses per fraction of 1 × 20 Gy and 3 × 15 Gy showed a reduction in $VVD_{25-35\,\mu m}$ (figure 5(D)) that reached a nadir at ∼2–4 weeks however only the 3 × 15 Gy treated mice reached a statistically significant difference compared to controls. The 1 × 20 Gy and 3 × 15 Gy treated mice had a significant reduction in $VVD_{15-25\mu m}$ that reached a nadir at ∼3 weeks (figure 5(E)). After this, the small vessels regrew and recovered to pre-irradiation levels by 7 weeks for both 1 × 20 Gy and 3 × 15 Gy treated tumours. Regrowth in the

microvasculature after high dose radiation ablation has been observed in several other studies (Kozin *et al* 2012, Park *et al* 2012, Demidov *et al* 2018a), however the precise impact of HDFRT on small *versus* large vessels, particularly over a monitoring period of 7 weeks as presented here, has not been studied.

It is generally accepted that doses >10 Gy are needed for most tumours to experience some form of microvascular ablation (Fuks and Kolesnick 2005). Interestingly, our results suggest that delivering 10 Gy (even repeated 3 times per week) was still not sufficient to induce microvascular ablation in these tumours, so the 'threshold dose' for microvascular response must be higher here. Treatments schedules with a higher dose per fraction of >10 Gy (1×20 Gy and 3×15 Gy) did indeed result in vascular ablation (figures 5(D) and (E)). These findings suggest that the dose per fraction is more important for inducing microvascular ablation rather than the total delivered dose. However, the total delivered dose seems to be an important determinant of the diameter of vessels that are ablated: the 3×15 Gy treated mice exhibited significant ablation of the 15–35 μm diameter vessels, yet only the smaller 15–25 μm diameter vessels were ablated in the 1×20 Gy cohort. It is also possible that the level of microvascular ablation may depend on the time between fractions (e.g., irradiation every day *versus* every other day). Further experiments with different fractionation schedules are needed to further explore the parameter space of dose/fraction, total delivered dose, and time between fractions for their impacts on the tumour microvasculature (Arnold *et al* 2018). Additionally, the drop in $VVD_{25-35\mu m}$ and $VVD_{15-25\mu m}$ (figures 5(D) and (E)) on day four of the 3×15 Gy schedule, although only on the verge of statistical significance, may suggest that increasing the time between the second and third fraction could improve treatment outcome by allowing for possible vascular regrowth and reoxygenation (Jeong *et al* 2013). Overall, these microvascular changes appear to have no impact on the tumour response (measured by tumour volume (figure 5(A)) and fluorescence (figure 5(B))) since all treatment schedules lead to a similar level of tumour control; however it is likely that the monitoring period was too short or radiobiological saturation was reached.

3.2. HDFRT impact on microvascular organization

Baish *et al* developed a new microvascular metric called the convexity index λ to describe the shape of avascular regions (Baish *et al* 2011). They demonstrated that plotting the log–log distance to the nearest vessel histogram, $n(\delta)$, for tumour and healthy tissue yielded significantly different histogram shapes. Specifically, the slope of the initial linear portion of the histogram, λ, describes the organization of the extravascular space and is related to the efficiency of the vascular network. Healthy tissue, with well-organized microvasculature, exhibited a positive initial slope with a rapid drop off as the maximum distance to the nearest vessel is reached. This is indicative of a concave avascular space geometry which is well suited for efficient nutrient and oxygen delivery to the surrounding tissue (Baish *et al* 2011). On the other hand, tumours had a downward sloping histogram indicating a convex avascular space geometry with avascular holes of varying sizes. The negative λ and convex geometry was indicative of malformed vessel organization leading to poorly perfused and hypoxic regions (Baish *et al* 2011).

Figure 6(A) shows λ over time for the control and treated tumours. The $n(\delta)$ histogram with its convexity index slope λ is displayed for a representative tumour from each cohort at day 0 and at 7 weeks (figures 6(B)–(E)). The wide range of starting λ_0 values shown in figures 6(B)–(E) is representative of the biological variation in these datasets, and this explains our rationale for displaying the relative percentage change in the longitudinal plot (figure 6(A)).

Unirradiated control tumours exhibited a consistent decrease in λ over time (becoming more negative), indicating that the microvascular network is continuing to become more chaotic and unorganized (figure 6(A)). This is shown in figure 6(B) as λ changes from -0.35 at day 0 to -0.64 at 7 weeks. 3×10 Gy treated tumours also experienced a decrease in λ over time, consistent with there being no impact on the microvasculature for this fractionation schedule (figures 5(C)–(E) and 6(A)). In the representative 3×10 Gy tumour shown in figure 6(C), λ becomes more negative (-0.38 at day 0 to -0.68 at 7 weeks) indicating a progressively worsening microvascular organizational structure similar to control tumours.

Treatments that did elicit a microvascular ablation response (1×20 Gy and 3×15 Gy, see figures 5(D) and (E)) had a significantly higher λ (i.e., less negative) compared to controls at 7 weeks (figure 6(A)). The 1×20 Gy treated tumour in figure 6(D) and the 3×15 Gy treated tumour in figure 6(E) approximately maintained, or slightly increased, their λ values from 0 to 7 weeks. In concert with our findings that 1×20 Gy and 3×15 Gy tumours experienced ablation in small microvessels (diameter between $15-25$ μm) followed by regrowth (figure 5(E)), we posit that the *regrown* microvasculature is more organized than the control unirradiated mice at 7 weeks. These findings are consistent with our previous work showing that high single dose irradiations of 20 and 30 Gy led to an increase in λ relative to day 0 by 7 weeks (Allam *et al* 2022). These findings also align with other groups that have identified reduced hypoxia (Samuel *et al* 2024) and potentially more normalized vasculature (Clément-Colmou *et al* 2020, Kaeppler *et al* 2022) following HDFRT.

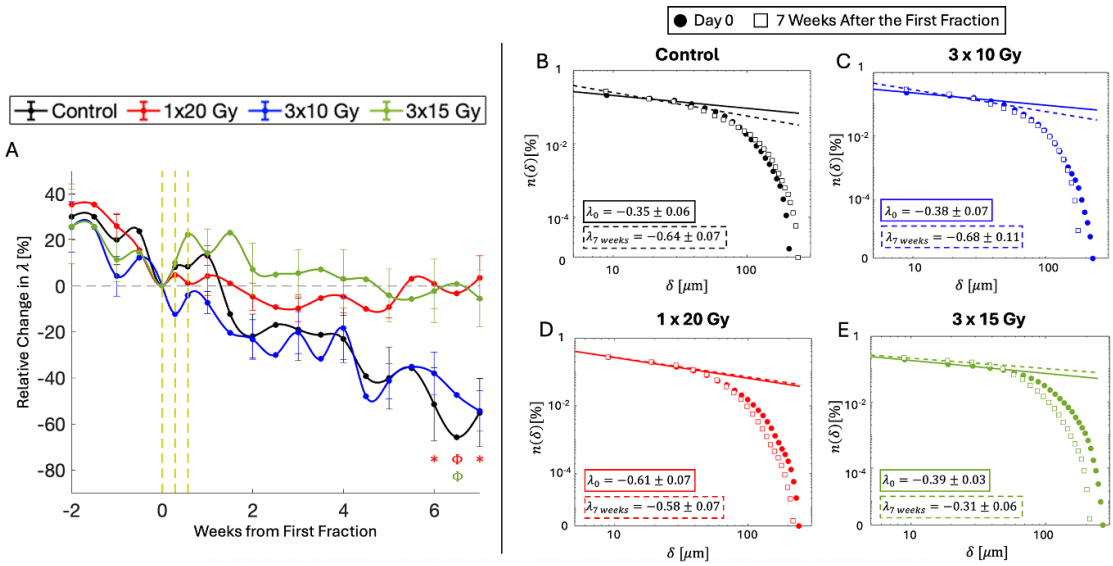

Figure 6. Response of the convexity index λ to different HDFRT irradiation schedules. (A) Percentage changes in λ relative to the day 0 pre-irradiation time point for control and HDFRT treated tumour cohorts. Points are mean values with error bars $\pm$SEM; symbols represent significant differences of the treatment cohorts vs. controls with the following significance levels: $^*p < 0.05$, Φ $p < 0.01$. (B)–(E) $n(\delta)$ log–log plots at day 0 (solid circles) and at 7 weeks (hollow squares) for a representative tumour from each cohort. (B)–(E) The solid line for day 0 and dotted line for 7 weeks represent the linear fit to the data for $\delta \leq 40$ μm and the slopes of these lines (λ) are displayed with the associated fitting uncertainty.

To help interpret the results, consider that Jain *et al* have proposed a 'vascular normalization' hypothesis, whereby the administration of antiangiogenic drugs such as a VEGF blockades, often at sub-therapeutic dose levels, could induce a more normal vascular structure (by disabling the most dysfunctional regions of the abnormal tumour vascularity) and lead to increased tumour perfusion and thus enhanced treatment response for subsequent therapies (Goel *et al* 2012). In our case, HDFRT may indeed be acting as an antiangiogenic therapy (while also contributing to direct tumour cell kill by DNA damage). The improved vessel organization in 1×20 Gy and 3×15 Gy treated mice at 7 weeks compared to controls suggests that subsequent delivery of anticancer drugs, chemotherapy, or radiotherapy might prove more effective (Huang *et al* 2013).

The trends in λ may also help to explain the tumour volume and fluorescence trends of the control cohort seen in figures 5(A) and (B). For example, starting at ~4 weeks, the control tumour volume (figure 5(A)) grows whereas the fluorescence (figure 5(B)) stops increasing and stagnates. This may be interpreted with the help of the observed λ behaviour which exhibited a steady decrease in λ for control mice (figure 6(A)); this decrease may indicate that the tumour cells, although still growing, may be less well blood-supplied and thus less viable resulting in a stagnation in the fluorescence. An alternative explanation is that as the tumour grows, there is a larger non-fluorescing stromal compartment which will lead to an increase in tumour volume without a corresponding increase in overall fluorescence.

3.3. Limitations and future work

A limitation of this study is that it does not identify *how* microvascular changes are impacting the response of the tumour to the treatment; we are rather just documenting and measuring the tumour microvascular, viability, and volume changes over time. Other studies may offer some useful insights to address the linkage between vascular damage and tumour volume change. For example, Castel *et al* used genetically engineered mouse models to differentially radiosensitize tumour cells and endothelial cells, demonstrating that endothelial cell death leads to tumour regrowth delay (delayed volume change) but not local control in HDFRT (Castle and Kirsch 2019). Additionally, Brown *et al* argue that the classical LQ model remains applicable to HDFRT, implying that tumour response is governed primarily by traditional cellular DNA damage mechanisms without significant microvascular involvement (2014). Kaeppler *et al* reported that only dysfunctional vessels were ablated during HDFRT, which may limit the impact of vascular changes on tumour cell kill and thus overall tumour volume (2022). In accord with these findings, we also did not observe differential tumour response despite different microvascular changes between the fractionation schedules, suggesting perhaps an overall limited role of the microvasculature in HDFRT. That said, other studies suggest otherwise (Kirkpatrick *et al* 2008, Kim *et al* 2015). Further, possible effects of monitoring period length and radiobiological saturation (as mentioned previously) may play a role here.

The generalizability of these findings is limited given that a single human tumour type in the dorsal skin of immunodeficient mice was employed. We used the DSWC model since it has been optimized for long term repetitive imaging of the tumour microvascular response, also allowing direct comparison with our previous work (Mariampillai *et al* 2008, 2010, Demidov *et al* 2018a, Allam *et al* 2022). More biologically realistic orthotopic models such as the pancreatic abdominal window chamber model (Samuel *et al* 2024) show promise for microvascular response monitoring, but are prone to motion artefacts. Different human tumour types as well as syngeneic mouse tumour models are also an important avenue of future research to better understand the role of the immune system response in HDFRT (Kozin 2022). Nevertheless, our findings that small vessels are more sensitive to HDFRT has been corroborated in several other tumour types and animal models (Solesvik *et al* 1984, Bouchet *et al* 2015, Kaeppler *et al* 2022).

The VVD metric is a rather simplistic first-order description of the complex 3D structure of the vascular network. Even with its refinement for small vessels as explored in this study, many other metrics could be examined for radiotherapeutic monitoring to provide additional insight into the morphological microvascular changes such as tortuosity (a measure vessel organization) (Conroy *et al* 2012), average intervascular distance (a surrogate for hypoxia) (Zabel *et al* 2022, 2024), and fractal dimension (quantification of vascular space filling) (Baish and Jain 2000). Artificial intelligence methods for RT microvascular response quantification have also shown promise (Majumdar *et al* 2022).

There are clearly significant biological variations in microvascular response between different studies (Park *et al* 2012, Kozin 2022) and even within our own group (Demidov *et al* 2018a) despite the controlled nature of these experiments. The variability in 'real-life' human clinical scenarios must also be immense considering different tumour sites and individual patient characteristics (Metran-Nascente *et al* 2016). To address this, we believe that individual patient microvascular imaging and quantification must be performed in the clinic to best optimize treatment. Such treatment optimizations could include altering the fractionation schedule to allow for vessel growth and tumour cell reoxygenation (Jeong *et al* 2013) or selectively targeting dose to hypoxic regions of the tumour (Bentzen and Gregoire 2011). To enable this, we must (1) have the necessary imaging methods to quantify the microvascular structure in a clinical setting (McDonald and Choyke 2003), and (2) determine how specific microvascular structures impact treatment response. Our group (Zabel *et al* 2022, 2024) and others (Gaustad *et al* 2008, Reitan *et al* 2010) have made progress in addressing (1) by directly correlating high resolution intravital microscopy images (svOCT and beyond) with more clinically applicable (but microvascularly-unresolved) perfusion MR; however, more studies must be done to address (2). Particularly, preclinical studies where the treatment schedule is adjusted based on the individual status of the tumour microvasculature should be performed to identify patient specific treatment adjustments to improve outcome.

4. Conclusion

This work supports emerging evidence that the tumour microvasculature is ablated by HDFRT; however, the dose per fraction and total delivered dose may determine whether ablation occurs and the size of vessels that are ablated. In this study, we found that 1×20 Gy ablated vessels with diameters between 15–25 μm, 3×15 Gy affected 15–35 μm diameter vessels, and 3×10 Gy treated mice exhibited no vascular ablation. We also found that the ablated microvessels regrew in a more organized fashion following treatments compared to controls as measured by the convexity index λ. The tumour volume and cell viability response at 7 weeks was similar for all treated tumours. Future work should aim to further identify the impact of these microvascular changes on tumour response and how changes in the fractionation schedule lead to different microvascular responses. Finally, individual patient microvascular imaging in the clinic could prove useful in light of the extensive microvascular heterogeneity and tumour responses to HDFRT regimens found in both preclinical and clinical studies.

Data availability statement

The data that support the findings of this study are available upon reasonable request from the authors.

Acknowledgment

The authors thank Rita Chen and Teesha Komal (STTARR facility, Princess Margaret Cancer Centre) for help with irradiation and treatment planning, Dr Shane Harding (Department of Medical Biophysics, University of Toronto) for discussions on the tumour volume response, Dr Valentin Demidov (Geisel School of Medicine, Dartmouth College) for discussions on data interpretation and methodology, and Dr Carla Calçada (Princess Margaret Cancer Centre) for help with cell culturing methodology. This research was

funded by the Canadian Institutes of Health Research (Grant # 202010PJT-451556-MPI-ADHD-40858). J Z, N A received funding from the Ontario Graduate Scholarship. J Z, H C, N A received funding from STARS21 program and the Princess Margaret Cancer Foundation.

Ethical statement

All animal procedures were performed in accordance with the Guide to the Care and Use of Experimental Animals set forth by the Canadian Council on Animal Care. The experimental protocol was approved by the University Health Network Institutional Animal Care and Use Committee in Toronto, Canada (animal use protocol #3256).

Conflict of interest

The authors declare no competing interests.

ORCID iDs

W Jeffrey Zabel https://orcid.org/0009-0002-6401-5634
Hector A Contreras-Sanchez https://orcid.org/0009-0007-8147-0483
Muhammad Mohsin Qureshi https://orcid.org/0000-0003-0362-0144
Costel Flueraru https://orcid.org/0000-0001-9334-6163
Edward Taylor https://orcid.org/0000-0001-7374-0390
I Alex Vitkin https://orcid.org/0000-0001-5495-8888

References

Allam N, Zabel W J, Demidov V, Jones B, Flueraru C, Taylor E and Vitkin I A 2022 Longitudinal *in-vivo* quantification of tumour microvascular heterogeneity by optical coherence angiography in pre-clinical radiation therapy *Sci. Rep.* **12** 6140
Arnold K M, Flynn N J, Raben A, Romak L, Yu Y, Dicker A P, Mourtada F and Sims-Mourtada J 2018 The impact of radiation on the tumor microenvironment effect of dose and fractionation schedules *Cancer Growth Metastasis* 11
Baish J W and Jain R K 2000 Fractals and cancer *Cancer Res.* **60** 3683–8
Baish J W, Stylianopoulos T, Lanning R M, Kamoun W S, Fukumura D, Munn L L and Jain R K 2011 Scaling rules for diffusive drug delivery in tumor and normal tissues *Proc. Natl Acad. Sci. USA* **108** 1799–803
Bentzen S M and Gregoire V 2011 Molecular imaging-based dose painting a novel paradigm for radiation therapy prescription *Semin. Radiat. Oncol.* **21** 101–10
Bouchet A, Serduc R, Laissue J A and Djonov V 2015 Effects of microbeam radiation therapy on normal and tumoral blood vessels *Phys. Med.* **31** 634–41
Brown J M, Carlson D J and Brenner D J 2014 The tumor radiobiology of SRS and SBRT are more than the 5 Rs involved? *Int. J. Radiat. Oncol. Biol. Phys.* **88** 254–62
Carlson D J, Keall P J, Bw L Jr, Chen Z J and Brown J M 2011 Hypofractionation results in reduced tumor cell kill compared to conventional fractionation for tumors with regions of hypoxia *Int. J. Radiat. Oncol. Biol. Phys.* **79** 1188–95
Casper M, Schulz-Hildebrandt H, Evers M, Birngruber R, Manstein D and Hüttmann G 2019 Optimization-based vessel segmentation pipeline for robust quantification of capillary networks in skin with optical coherence tomography angiography *J. Biomed. Opt.* **24** 1–11
Castle K D and Kirsch D G 2019 Establishing the impact of vascular damage on tumor response to high-dose radiation therapy *Cancer Res.* **79** 5685–92
Clark D P and Badea C T 2021 Advances in micro-CT imaging of small animals *Phys. Med.* **88** 175–92
Clément-Colmou K, Potiron V, Pietri M, Guillonneau M, Jouglar E, Chiavassa S, Delpon G, Paris F and Supiot S 2020 Influence of radiotherapy fractionation schedule on the tumor vascular microenvironment in prostate and lung cancer models *Cancers* **12** 121
Conroy L, DaCosta R S and Vitkin I A 2012 Quantifying tissue microvasculature with speckle variance optical coherence tomography *Opt. Lett.* **37** 3180–2
Cuenod C A and Balvay D 2013 Perfusion and vascular permeability basic concepts and measurement in DCE-CT and DCE-MRI *Diagn. Interv. Imaging* **94** 1187–204
Demidov V, Maeda A, Sugita M, Madge V, Sadanand S, Flueraru C and Vitkin I A 2018a Preclinical longitudinal imaging of tumor microvascular radiobiological response with functional optical coherence tomography *Sci. Rep.* **8** 38
Demidov V, Zhao X, Demidova O, Pang H Y M, Flueraru C, Liu F F and Vitkin I A 2018b Preclinical quantitative *in-vivo* assessment of skin tissue vascularity in radiation-induced fibrosis with optical coherence tomography *J. Biomed. Opt.* **23** 1–9
Ferrara N 2005 VEGF as a therapeutic target in cancer *Oncology* **69** 11–16
Fitzpatrick J M and Sonka M 2000 *Handbook of Medical Imaging, Volume 2: Medical Image Processing and Analysis* (SPIE Press Book)
Fuks Z and Kolesnick R 2005 Engaging the vascular component of the tumor response *Cancer Cell* **8** 89–91
Gaustad J V, Brurberg K G, Simonsen T G, Mollatt C S and Rofstad E K 2008 Tumor vascularity assessed by magnetic resonance imaging and intravital microscopy imaging *Neoplasia* **10** 354–62
Goel S, Wong A H and Jain R K 2012 Vascular normalization as a therapeutic strategy for malignant and nonmalignant disease *Cold Spring Harb. Perspect. Med.* **2** a006486
Gueorguieva R and Krystal J H 2004 Move over ANOVA progress in analyzing repeated-measures data and its reflection in papers published in the Archives of General Psychiatry *Arch. Gen. Psychiatry* **61** 310–7
Huang Y, Stylianopoulos T, Duda D G, Fukumura D and Jain R K 2013 Benefits of vascular normalization are dose and time dependent *Cancer Res.* **73** 7144–6

Jenkinson M and Smith S 2001 A global optimisation method for robust affine registration of brain images *Med. Image Anal.* **5** 143–56
Jensen E C 2012 Use of fluorescent probes their effect on cell biology and limitations *Anat. Rec.* **295** 2031–6
Jeong J, Oh J H, Sonke J J, Belderbos J, Bradley J D, Fontanella A N, Rao S S and Deasy J O 2017 Modeling the cellular response of lung cancer to radiation therapy for a broad range of fractionation schedules *Clin. Cancer Res.* **23** 5469–79
Jeong J, Shoghi K I and Deasy J O 2013 Modelling the interplay between hypoxia and proliferation in radiotherapy tumour response *Phys. Med. Biol.* **58** 4897–919
Kaeppler J R *et al* 2022 Endothelial cell death after ionizing radiation does not impair vascular structure in mouse tumor models *EMBO Rep.* **23** e53221
Kim M S, Kim W, Park I H, Kim H J, Lee E, Jung J H, Cho L C and Song C W 2015 Radiobiological mechanisms of stereotactic body radiation therapy and stereotactic radiation surgery *Radiat. Oncol. J.* **33** 265–75
Kirkpatrick J P, Meyer J J and Marks L B 2008 The linear-quadratic model is inappropriate to model high dose per fraction effects in radiosurgery *Semin. Radiat. Oncol.* **18** 240–3
Kozin S V 2022 Vascular damage in tumors a key player in stereotactic radiation therapy? *Trends Cancer* **8** 806–19
Kozin S V, Duda D G, Munn L L and Jain R K 2012 Neovascularization after irradiation what is the source of newly formed vessels in recurring tumors? *J. Natl Cancer Inst.* **104** 899–905
Lin Q, Choyke P L and Sato N 2023 Visualizing vasculature and its response to therapy in the tumor microenvironment *Theranostics* **13** 5223–46
Liu C and Wang L 2022 Functional photoacoustic microscopy of hemodynamics a review *Biomed. Eng. Lett.* **12** 97–124
Maeda A and DaCosta R S 2014 Optimization of the dorsal skinfold window chamber model and multi-parametric characterization of tumor-associated vasculature *Intravital* **3** e27935
Majumdar A, Allam N, Zabel W J, Demidov V, Flueraru C and Vitkin I A 2022 Binary dose level classification of tumour microvascular response to radiotherapy using artificial intelligence analysis of optical coherence tomography images *Sci. Rep.* **12** 13995
Mao Y, Sherif S, Flueraru C and Chang S 2008 3 × 3 Mach-Zehnder interferometer with unbalanced differential detection for full-range swept-source optical coherence tomography *Appl. Opt.* **47** 2004–10
Mariampillai A *et al* 2008 Speckle variance detection of microvasculature using swept-source optical coherence tomography *Opt. Lett.* **33** 1530–2
Mariampillai A, Leung M K, Jarvi M, Standish B A, Lee K, Wilson B C, Vitkin A and Yang V X 2010 Optimized speckle variance OCT imaging of microvasculature *Opt. Lett.* **35** 1257–9
McDonald D M and Choyke P L 2003 Imaging of angiogenesis from microscope to clinic *Nat. Med.* **9** 713–25
Mendonça A M and Campilho A 2006 Segmentation of retinal blood vessels by combining the detection of centerlines and morphological reconstruction *IEEE Trans. Med. Imaging* **25** 1200–13
Menger M D, Laschke M W and Vollmar B 2002 Viewing the microcirculation through the window some twenty years experience with the hamster dorsal skinfold chamber *Eur. Surg. Res.* **34** 83–91
Metran-Nascente C, Yeung I, Vines D C, Metser U, Dhani N C, Green D, Milosevic M, Jaffray D and Hedley D W 2016 Measurement of tumor hypoxia in patients with advanced pancreatic cancer based on 18F-fluoroazomyin arabinoside uptake *J. Nucl. Med.* **57** 361–6
Moding E J, Clark D P, Qi Y, Li Y, Ma Y, Ghaghada K, Johnson G A, Kirsch D G and Badea C T 2013 Dual-energy micro-computed tomography imaging of radiation-induced vascular changes in primary mouse sarcomas *Int. J. Radiat. Oncol. Biol. Phys.* **85** 1353–9
Moran C M and Thomson A J W 2020 Preclinical ultrasound imaging—a review of techniques and imaging applications *Front. Phys.* **8** 124
Muz B, de la Puente P, Azab F and Azab A K 2015 The role of hypoxia in cancer progression, angiogenesis, metastasis, and resistance to therapy *Hypoxia (Auckl)* **3** 83–92
Otsu N 1979 A threshold selection method from gray-level histograms *IEEE Trans. Syst. Man Cybern.* **9** 62–66
Park H J, Griffin R J, Hui S, Levitt S H and Song C W 2012 Radiation-induced vascular damage in tumors implications of vascular damage in ablative hypofractionated radiotherapy (SBRT and SRS) *Radiat. Res.* **177** 311–27
Park J J *et al* 2017 Stereotactic body radiation vs. intensity-modulated radiation for unresectable pancreatic cancer *Acta Oncol.* **56** 1746–53
Reitan N K, Thuen M, Goa P E and de Lange Davies C 2010 Characterization of tumor microvascular structure and permeability comparison between magnetic resonance imaging and intravital confocal imaging *J. Biomed. Opt.* **15** 036004
Samuel T, Rapic S, Lindsay P E and DaCosta R S 2024 Investigating the effects of stereotactic body radiation therapy on pancreatic tumor hypoxia and microvasculature in an orthotopic mouse model using intravital fluorescence microscopy *Sci. Rep.* **14** 31348
Schreiter J, Meyer S, Schmidt C, Schulz R M and Langer S 2017 Dorsal skinfold chamber models in mice *GMS Interdiscip. Plast. Reconstr. Surg. DGPW* **6** Doc10
Solesvik O V, Rofstad E K and Brustad T 1984 Vascular changes in a human malignant melanoma xenograft following single-dose irradiation *Radiat. Res.* **98** 115–28
Suetsugu A, Katz M, Fleming J, Truty M, Thomas R, Saji S, Moriwaki H, Bouvet M and Hoffman R M 2012 Non-invasive fluorescent-protein imaging of orthotopic pancreatic-cancer-patient tumorgraft progression in nude mice *Anticancer Res.* **32** 3063–7
Tan M H, Nowak N J, Loor R, Ochi H, Sandberg A A, Lopez C, Pickren J W, Berjian R, Douglass H O Jr and Chu T M 1986 Characterization of a new primary human pancreatic tumor line *Cancer Invest.* **4** 15–23
Timmerman R D, Herman J and Cho L C 2014 Emergence of stereotactic body radiation therapy and its impact on current and future clinical practice *J. Clin. Oncol.* **32** 2847–54
Vakoc B J *et al* 2009 Three-dimensional microscopy of the tumor microenvironment *in vivo* using optical frequency domain imaging *Nat. Med.* **15** 1219–23
van Hoof S J, Granton P V and Verhaegen F 2013 Development and validation of a treatment planning system for small animal radiotherapy SmART-Plan *Radiother. Oncol.* **109** 361–6
Zabel W J, Allam N, Contreras Sanchez H A, Foltz W, Flueraru C, Taylor E and Vitkin A 2024 A dorsal skinfold window chamber tumor mouse model for combined intravital microscopy and magnetic resonance imaging in translational cancer research *J. Vis. Exp.* **206** e66383
Zabel W J, Allam N, Foltz W D, Flueraru C, Taylor E and Vitkin I A 2022 Bridging the macro to micro resolution gap with angiographic optical coherence tomography and dynamic contrast enhanced MRI *Sci. Rep.* **12** 3159